

pubs.acs.org/Biomac Article

Concentration-Independent Multivalent Targeting of Cancer Cells by Genetically Encoded Core-Crosslinked Elastin/Resilin-like Polypeptide Micelles

Patrick Weber, Michael Dzuricky, Junseon Min, Irene Jenkins, and Ashutosh Chilkoti*



Cite This: Biomacromolecules 2021, 22, 4347-4356



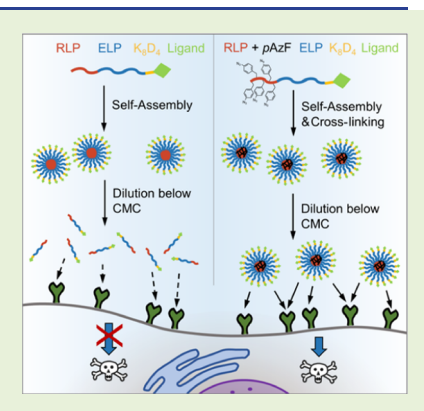
ACCESS

III Metrics & More



Supporting Information

ABSTRACT: Valency is a fundamental principle to control macromolecular interactions and is used to target specific cell types by multivalent ligand—receptor interactions using self-assembled nanoparticle carriers. At the concentrations encountered in solid tumors upon systemic administration, these nanoparticles are, however, likely to show critical micelle concentration (CMC)-dependent disassembly and thus loss of function. To overcome this limitation, core-crosslinkable micelles of genetically encoded resilin-/elastin-like diblock polypeptides were recombinantly synthesized. The amphiphilic constructs were covalently photo-crosslinked through the genetically encoded unnatural amino acid *para*-azidophenylalanine in their hydrophobic block and they carried different anticancer ligands on their hydrophilic block: the wild-type tenth human fibronectin type III domain, a GRGDSPAS peptide—both targeting $\alpha_v \beta_3$ integrin—and an engineered variant of the third fibronectin type III domain of tenascin C that is a death receptor 5 agonist. Although uncrosslinked micelles lost most of their targeting ability below their CMC, the crosslinked analogues remained active at concentrations up to 1000-fold lower than the CMC, with binding affinities that are comparable to antibodies.



INTRODUCTION

The past three decades have seen a dramatic increase in the number of nanoparticle-based delivery systems that have been developed to improve the delivery of therapeutic drugs and/or diagnostic markers.^{1,2} These systems were largely limited to liposomes and lipid emulsions until the 1990s,^{3/5} but since then many more nanoscale delivery vehicles have been developed such as solid lipid nanoparticles, polymersomes, polymer micelles, inorganic nanoparticles, and dendrimers. 6-9 These delivery systems greatly increase the serum half-life of small molecule drugs and can improve targeting to the diseased tissue. 10 In cancer therapy, these nanoparticle carriers provide an added benefit, as their size (10-200 nm) has been associated with higher uptake rates into solid tumors compared to other tissues. 11,12 Moreover, active targeting of tumors by nanoparticles that present tumor-selective ligands can enhance the delivery of small molecule drugs conjugated to or sequestered within the nanoparticles compared to non-targeted analogues.¹³ Depending on the choice of the ligand, receptor engagement by the ligand can itself modulate intracellular signaling pathways in cancer cells, leading to the downregulation of oncogenes¹⁴ or the induction of apoptosis.¹⁵

Because nanoparticles often present multiple copies of a ligand on their surface, they can engage tumors cells by multivalent interactions—the simultaneous formation of multiple ligand—receptor bonds in close spatial proximity. Increasing ligand valency has been shown to not only improve

the tumor targeting by nanoparticles but to also promote induction of cell signaling cascades, for instance, by ligands targeting integrins, ¹⁶ death receptor 5 (DR5), ^{17,18} or transferrin receptors. ¹⁹ Typically, these multivalency-dependent effects proceed through signal amplification or by facilitating signal transduction, for instance, when receptor clustering is necessary on the cell membrane. ²⁰

However, this effect strongly depends on the stability of the particles, as the intratumoral concentration after passive accumulation must be high enough—relative to the avidity of the nanoparticles for the target receptor(s)—to enable multivalent engagement with the tumor cell surface receptors. This requires that the nanoparticles must remain assembled *in vivo* as they transit from the site of injection to the tumor microenvironment. This problem is especially acute for self-assembled nanoparticles that are held together by weak noncovalent interactions and exist in thermodynamic equilibrium between the self-assembled nanoparticles and their unimer building blocks. Upon dilution below their critical micelle concentration (CMC)—often in the micromolar to nanomolar

Received: July 13, 2021 Revised: August 20, 2021 Published: September 3, 2021





range in phosphate-buffered saline (PBS) and substantially higher in serum—they dissociate into unimers.^{21–24} Thus, the CMC of a nanoparticle is an important determinant of its *in vivo* performance, as renal excretion and tissue accumulation rapidly dilute the particles in circulation, leading to disassembly, loss of multivalency, and consequently loss of function.

This situation is further exacerbated by recent improvements in the design of anticancer ligands. Using computational design or library-based screening approaches, we now not only have the ability to engineer complex antibodies with femtomolar binding affinity^{25,26} but also simple peptides that have an affinity for their targets in the nanomolar range. 27,28 Their high avidity upon multivalent display, however, is irrelevant if the self-assembled nanocarriers disassemble at far higher concentrations. 18,29,30 One solution to this dichotomy is to introduce covalent crosslinks between the building blocks, thereby completely removing the CMC from the equation. Though several such systems, typically core-crosslinked polymer micelles, have already been created through in situ crosspolymerization,³¹ disulfide bridges,³² or boronate esters³³ and have shown to improve particle stability in circulation and improved tumor accumulation,³⁴ the impact on multivalency and tumor targeting has not been investigated in detail.³⁵

To fill this gap, we designed a genetically encoded diblock polypeptide construct consisting of elastin- and resilin-like polypeptides (ELPs/RLPs)—bioinspired and highly biocompatible materials—already being used for many biomedical applications. 30,36-39 ELP/RLP diblock copolypeptides also have the unique advantage that due to their recombinant nature, we have absolute control over the length and sequence of the individual blocks at the gene level, which allows the morphology of the self-assembled nanoparticles to be precisely modulated, which in turn dramatically influences the activity of the nanoparticles. 30,40 The construct for this study consists of a hydrophobic RLP block of 40 repeats of the octapeptide QYPSDGRG and a hydrophilic ELP block of 80 G[G:A]GVP repeats and is hereafter referred to as RLP₄₀-ELP₈₀. Previous studies on this diblock polypeptide have shown that it selfassembles into spherical micelles with a ~60 nm diameter and that its self-assembly into spherical micelles is not perturbed by the genetically encoded presentation of peptide and protein ligands on its corona. 30,40 To covalently crosslink the core of these micelles, we recombinantly introduced the unnatural amino acid *para*-azidophenylalanine (*p*AzF) into the coreforming RLP block. 41-44 By subsequent exposure to UV irradiation, the pAzF residues readily enter into any nearby N-H or C-H bonds, thereby forming irreversible intra- and intermolecular crosslinks. 45,46

In this study, we recombinantly presented three different anticancer ligands on the coronal end of the RLP/ELP micelles to create core-crosslinkable micelles that target the $\alpha_v \beta_3$ integrin and DR5 receptors that are commonly upregulated in many solid tumors. Direct comparison of crosslinked and uncrosslinked micelles showed that core crosslinking increases the potency of targeting by up to 3 orders of magnitude into a concentration range well below the CMC of the micelles and thus demonstrates the critical role of nanoparticle stability on multivalent activity.

MATERIALS AND METHODS

Materials. Competent BL21 (DE3) and NEB 5-alpha Escherichia coli strains were obtained from New England Biolabs (Ipswich, MA,

USA). Amber-suppressor C321.ΔA E. coli as well as the orthogonal pEVOL vector were generously provided by Prof. Farren J. Isaacs (Yale University, USA). Para-azidophenylalanine was supplied by Chem-Impex International (Wood Dale, IL, USA). Kanamycin sulfate was purchased from EMD Millipore (Billerica, MA, USA) and chloramphenicol from Sigma-Aldrich (St. Louis, MO, USA). Isopropyl β -D-1-thiogalactopyranoside (IPTG) was bought from Gold Biotechnology (St. Louis, MO, USA) and PBS tablets from Calbiochem (San Diego, CA, USA). Bacterial cultures were sonicated using a QSonica Q500 sonicator (Newtown, CT, USA) and purified with a Beckman Coulter J2-HC centrifuge equipped with a JA-20 rotor (cold spin, Beckman Coulter, Brea, CA, USA) as well as a Sorvall RC 5B centrifuge equipped with a SS34 rotor (Thermo Fisher Scientific, Waltham, MA, USA). SimplyBlue stain and NHS ester Alexa Fluor 488 dye were purchased from Thermo Fisher Scientific (Waltham, MA, USA). Sodium dodecyl sulfate polyacrylamide gel electrophoresis (SDS-PAGE) was performed using stain-free Mini-PROTEAN TGX precast gels and imaged on a Gel Doc XR+ imager both manufactured by Bio-Rad Laboratories (Hercules, CA, USA). Lyophilization was performed using a Labconco FreeZone 2.5 Plus lyophilizer (Labconco, Kansas City, MO, USA). Colo205 and K562 cells were bought from the American Type Culture Collection (ATCC, Manassas, VA, USA) and cultured following the instructions provided in their manuals on the ATCC website.

Vectors and Gene Assembly. The plasmid genes were assembled using the "plasmid reconstruction through recursive directional ligation" technique (PRe-RDL) described elsewhere.5 Most gene fragments were already available from previous experiments but if they were not, they were ordered as DNA oligonucleotides from Integrated DNA Technologies (Coralville, IA, USA) and inserted into the linearized PRe-RDL pET-24+ vector using the Gibson Assembly cloning kit supplied by New England Biolabs (Ipswich, MA, USA). During gene assembly exclusively, NEB 5-alpha competent E. coli were used for transformation and plasmid amplification. For native constructs containing no pAzF-encoding "TAG" codons, the fully assembled plasmid was transformed into BL21(DE3) competent E. coli for protein expression. For "TAG"positive, crosslinkable constructs, the assembled gene was transferred into a modified pET-24+ vector that does not contain AcuI, BseRI, and BglI restriction sites but has an pTAC promotor and rrnB terminator instead of the T7 equivalents.⁴¹ For the expression step, this plasmid was transformed into C321. DA competent E. coli that through a separate transformation already contained the pEVOL plasmid carrying the orthogonal tRNA/aaRS pair required for pAzFintroduction.

Protein Expression and Purification. For the pAzF-free constructs, protein expression was performed in 1 L 2xYT cultures (16 g/L tryptone, 10 g/L yeast extract, and 5 g/L NaCl) supplemented with kanamycin (45 $\mu g/mL$) using a 50 mL starter culture (grown overnight in the same medium at 37 °C and 210 rpm) to inoculate the flasks. The cultures were grown at 37 $^{\circ}\text{C}$ and 210 rpm in a shaker incubator. Once the cultures reached an OD_{600} of 0.6–0.8, IPTG was added to a final concentration of 1 mM. 24 h after inoculation, the cells were harvested from the suspension using centrifugation (3000 rpm for 10 min at 4 °C), resuspended in PBS and lysed by sonication on ice for 3 min (intervals of 10 s on and 40 s off). Subsequently, polyethyleneimine (0.7% w/v) was added to precipitate the nucleic acid contaminants, and the mixture was spun down (15,000 rpm for 30 min at 4 °C). The supernatant was purified by one round of inverse transition cycling (ITC). An inverse transition cycle comprises a hot and cold spin at solution conditions above and below the lower critical solution temperature phase transition of the constructs, respectively. For the hot spin, up to 3 M NaCl were added to isothermally trigger the phase transition of the RLP/ELP constructs and the coacervate was centrifuged at 15,000 rpm for 30 min at 37 $^{\circ}$ C. The supernatant was discarded and the pellet was resuspended on ice in deionized water. For the cold spin, the suspension was centrifuged at 15,000 rpm for 30 min at 4 °C and the supernatant was retained to complete one inverse transition cycle. The purity of the samples after one inverse transition cycle was

analyzed by SDS-PAGE and found to be >95% for all constructs investigated in this study. After purification by ITC, salt contaminants were removed by dialysis against deionized water over 36 h using SnakeSkin dialysis tubing (3500 MWCO, Thermo Fisher Scientific, Waltham, MA, USA). Finally, the samples were lyophilized and stored in aliquots at $-20~^{\circ}$ C until further use. The yield of the purified native—pAzF-free—RLP/ELP diblock polypeptide was \sim 50 mg/L of shaker flask culture.

For the pAzF-containing constructs, there were only a few differences to the expression and purification protocol described above: first, the growth medium contained three additional components [arabinose (0.2% w/v), chloramphenicol (25 μ g/mL), and para-azidophenylalanine (1 mM)]. Second, the cultures were grown at 34 °C before and at 25 °C after IPTG induction. Third, the samples were protected from UV light at all times to prevent premature crosslinking of the polypeptides. Finally, yields of purified polypeptide were typically lower at 5–25 mg/L of shaker flask culture.

Chemical Crosslinking. pAzF-containing polypeptides were crosslinked in PBS by exposure to high-intensity UV irradiation (OmniCure S1000 UV source with a 320–500 nm filter, Nordson Corporation, Westlake, OH, USA). Each sample was exposed to the UV source for three intervals of 20 s with mixing steps in between each exposure.

Dynamic Light Scattering. Dynamic light scattering (DLS) data was acquired using a DynaPro plate reader (Wyatt Technology, Goleta, CA, USA). Wells of a 96-well plate were loaded with 50 μ L of analyte solution and covered with mineral oil (25 μ L) to prevent solvent evaporation. The measurements were analyzed by fitting the autocorrelation function with a Rayleigh sphere cumulant fit model to determine R_b .

Zeta Potential Measurements. The zeta potential measurements were performed on a Malvern Zetasizer instrument (Malvern Panalytical, Malvern, UK) using 15 μ M solutions of diblock constructs in deionized water at 25 °C. The samples were loaded into a disposable folded capillary cell (DTS1070, Malvern Panalytical, Malvern, UK) and the zeta potential determined over five technical replicates per sample. To check if the nanoparticles had formed analogously in deionized water as in PBS, the $R_{\rm h}$ was measured analogously as described above. Finally, the pH of the sample solutions was also determined on an Orion Star A211 pH meter (Thermo Fisher Scientific, Waltham, MA, USA) to ensure comparability between the individual samples.

Cryogenic Transmission Electron Microscopy. Cryogenic transmission electron microscopy (Cryo-TEM) images were taken using a FEI Tecnai G2 Twin transmission electron microscope (FEI, Hillsboro, OR, USA) at a voltage of 80 kV. Prior to imaging, the samples were prepared as follows: lacey holey carbon grids (Ted Pella, Redding, CA, USA) were glow discharged using a PELCO easiGlow apparatus (Ted Pella, Redding, CA, USA) and loaded into a Vitrobot Mark IV vitrification instrument (FEI, Hillsboro, OR, USA). Subsequently, 3 μ L of the sample was carefully deposited onto the grid, blotted for 3 s at a force of -3 and with a drain time of 1 s and then vitrified in liquid ethane. The grids were transferred onto a Gatan 626 cryoholder (Gatan, Pleasanton, CA, USA) which was inserted into the TEM instrument.

AF488 Labeling. To obtain AF488-labeled proteins, some lyophilized protein sample was dissolved in aq sodium bicarbonate solution (0.1 M and pH, 8.3) to which the NHS ester derivative of the AF488 dye (Invitrogen, Carlsbad, CA, USA) was added in large excess (>5 equiv). After incubation at room temperature for 1 h, the sample was dialyzed and lyophilized analogously as for regular protein purification.

Cell Uptake Experiments. Cell uptake experiments were run using samples with a protein-to-dye ratio of 10:1 determined using a NanoDrop 1000 instrument (Thermo Fisher Scientific, Waltham, MA, USA). Protein samples (typically 100–500 μL) were then mixed with spun down K562 cells (500 g for 5 min) to reach a final density of 1 million cells/mL. After coincubation for 2 h at 37 °C and 200 rpm, the mixture was spun down at 800 g for 5 min and the supernatant was carefully removed. After two washing steps

(resuspension in 1 mL of Hanks' buffered salt solution, centrifugation at 1000g for 7 min and removal of the supernatant), the cell pellet was finally resuspended in PBS + 1% bovine serum albumin at a cell density of 1 million cells/mL. To analyze the cellular uptake levels, 30 μ L of the sample was loaded onto a 384-well plate with a #1.5 coverslip at the bottom and imaged using the 40× oil-immersion objective on a Dragonfly 500 spinning disk confocal microscope (Andor Technology, Belfast, UK). Moreover, cell uptake levels were also quantified on an Accuri C5 flow cytometer (Becton Dickinson, Franklin Lakes, NJ, USA). The cell fluorescence intensity was quantified after gating to remove false positive measurements.

Surface Plasmon Resonance. The surface plasmon resonance (SPR) measurements were carried out using a Biacore T200 instrument (GE Healthcare, Chicago, IL, USA) at 25 °C. The flow channels of the CM5 sensor chip (GE Healthcare, Chicago, IL, USA) were normalized using 70% glycerol. Recombinant $\alpha_v \beta_3$ integrins (Novus Biologicals, Littleton, CO, USA) were immobilized using NHS/EDC coupling. Upon immobilization, the integrins reached a surface density of around 1200 response units (RU). For the control channel, analogous methods were used to immobilize the crosslinked, unfunctionalized RLP20-ELP80 construct to reach a surface density of around 4500 RU. The SPR measurements were carried out using crosslinked and uncrosslinked nanoparticles at various concentrations in PBS. All samples were injected into the flow cells at a flow rate of 5 $\mu L/min$ for 3 min and then allowed to dissociate for 10 min. The surface was subsequently regenerated using 2 mM aq NaOH at a flow rate of 5 μ L/min for 40 s. After subtraction of the signal from the reference channel, the final SPR sensorgrams were analyzed using the 1:1 Langmuir binding model on BIAevaluation software (GE Healthcare, Chicago, IL, USA).

Cell Viability Assays. Wells of a 96-well plate were seeded with 10,000 Colo205 cells each in complete growth media (90 μ L, RPMI + 10% v/v fetal bovine serum). After 24 h of incubation at 37 °C, 10 μ L of protein sample in PBS was added in duplicates. After 24 h, 15 μ L of CellTiter-Glo (Promega Corporation, Madison, WI, USA) was added to each well and mixed by gently tapping the 96-well plate. After 40 min of incubation at room temperature under exclusion of light, cell viability was determined by measuring the luminescence of each well on a PerkinElmer Wallac 1420 VICTOR2 microplate reader (PerkinElmer, Waltham, MA, USA).

■ RESULTS AND DISCUSSION

To introduce pAzF residues into RLP_{40} — ELP_{80} , we genetically engineered five regularly spaced UAG amber codons into the RLP block, using a previously described recursive ligation cloning strategy. The resulting construct—hereafter referred to as $RLP_{40,5pAzF}$ — ELP_{80} —was expressed in a genetically recoded, amber-suppressor E. coli in shaker flask culture and isolated using ITC with a yield of \sim 40 mg/L of purified polypeptide. To prove successful incorporation of free azides, we incubated the purified polypeptide with a DBCO-functionalized fluorophore, yielding a single fluorescent band at the target mass of 66 kDa as seen by SDS-PAGE (Figure S1).

DLS measurements of RLP_{40} – ELP_{80} and $RLP_{40,5pAzF}$ – ELP_{80} in both uncrosslinked and crosslinked states yielded hydrodynamic radii (R_h) of 28–35 nm, which is in agreement with previous studies (Table 1). Though the differences are small, there is a trend toward an increase in size upon introduction of the pAzF residues as well as upon crosslinking of the particles, most probably due to minor rearrangements in the particle core. Further characterization of the particles by zeta potential measurements (Table S1) and cryo-TEM (Figure S2a) showed that both the interfacial properties as well as the spherical morphology of the particles remained unaffected by pAzF introduction and crosslinking.

Table 1. DLS characterization of unfunctionalized RLP/ELP nanoparticles before and after photo-crosslinking: Measurements were performed at 25 °C at a concentration of 15 μ M in PBS. $R_{\rm h}$: hydrodynamic radius

diblock architecture	sample state	pAzF residues	$R_{\rm h}$ [nm]
RLP ₄₀ -ELP ₈₀	uncrosslinked	no	28.0 ± 1.0
RLP ₄₀ -ELP ₈₀	uncrosslinked	yes	29.8 ± 0.2
$RLP_{40}-ELP_{80}$	crosslinked	yes	34.3 ± 0.3

To analyze how photo-crosslinking affected the stability of the micelles, we exposed both uncrosslinked and crosslinked RLP $_{40,5pAzF}$ -ELP $_{80}$ samples to 7.2 M guanidinium hydrochloride (GuHCl), a potent chemical denaturant. Subsequent DLS (Figure S2b) and cryo-TEM (Figure 1) demonstrated that the crosslinked nanoparticles retained their spherical morphology upon GuHCl exposure, whereas the uncrosslinked nanoparticles disassembled into unimers, as seen by the lack of nanoparticles in the cryo-TEM field of view. The observed swelling of the crosslinked particles in GuHCl can be attributed to the denaturing agent dissolving the phase-separated RLP core, thereby also causing a decrease in contrast in the cryo-TEM images.

To determine how many pAzF residues were actually necessary to create stable particles, we performed analogous stability tests with crosslinked mixed micelles containing pAzF free and pAzF-carrying RLP_{40} – ELP_{80} constructs at different ratios. The cutoff was found to be at an average of 1 pAzF residue per polypeptide chain (Figure S3). Finally, by acquiring DLS measurements over a dilution series of the RLP_{40} – ELP_{80} construct, its CMC was estimated to be $\sim 1~\mu\text{M}$ (Figure S4).

Motivated by these results for the unfunctionalized polypeptides, we designed RLP_{40,5pAzF}-ELP₈₀ constructs carrying anticancer ligands on their C-terminal, hydrophilic

end. There were two basic requirements that dictated the choice of the ligands for this study: first, the ligands needed to be sufficiently potent—at least in their multivalent form—such that the induced effects upon receptor binding were still detectable with our assays even at mid-nanomolar concentrations below the CMC. Second, the mono- and multivalent form of the ligand needed to be significantly different in activity for us to clearly be able to experimentally differentiate between the two states.

The first ligand we chose that fulfilled both criteria was a single domain protein based on the third type III fibronectin domain of tenascin C (Tn3) that had been engineered to bind to the apoptosis-inducing DR5, a systematically upregulated cell surface receptor in cancer cells (Figure 2). In the initial publication, mono- and divalent constructs of this ligand failed to show any cytotoxic effect, whereas tetra-, hexa-, and octameric constructs showed picomolar efficacy. The strong dependence of function on the multivalent display is thought to arise from the requirement for trimerization of DR5-receptors to trigger the downstream signaling pathway that ultimately leads to apoptotic cell death. We have previously reported on a depot-forming, linear ELP-(Tn3)₆ fusion construct with improved *in vivo* activity over monomeric TRAIL—the current gold-standard DR5 agonist. SS

The second and third ligand we chose both contain an RGD tripeptide motif (Figure 2). RGD ligands are amongst the most commonly used ligands for tumor targeting as their molecular targets—multiple members of the integrin family 56 —have been shown to be upregulated in many different types of cancer. They are also one of the most widely investigated ligands in the context of multivalent display. The two ligands we chose were the wild-type tenth type III domain from human fibronectin (Fn3) that shows binding specificity for the $\alpha_{\nu}\beta_{3}$ integrin 59 which is known to be highly

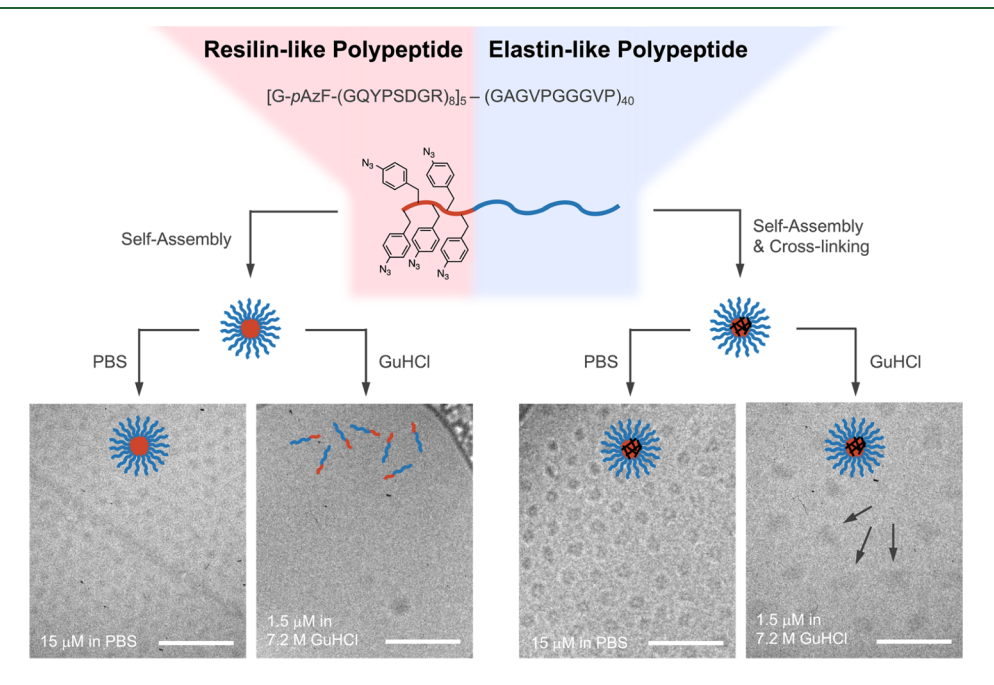


Figure 1. Construct overview and stability analysis of unfunctionalized RLP/ELP nanoparticles before and after photo-crosslinking: to enable photo-crosslinking, the diblock polypeptide contained 5 evenly spaced *p*AzF residues in the RLP block. Successful crosslinking was shown by incubation of nanoparticles with 7.2 M GuHCl: cryo-TEM micrographs show that crosslinked samples (particles indicated by arrows) retained their spherical morphology upon exposure to GuHCl, whereas the uncrosslinked nanoparticles disassembled into unimers that are not detectable by cryo-TEM. Scale bars represent 200 nm.

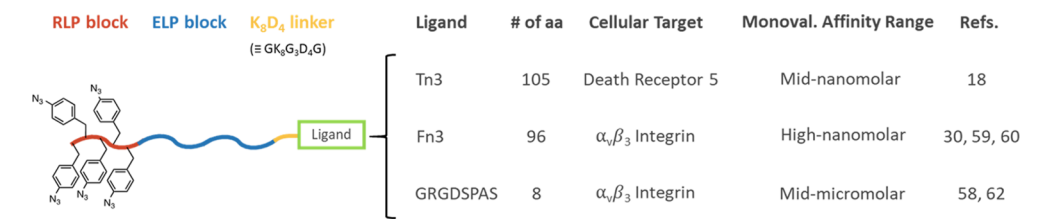


Figure 2. Architecture of the ligand functionalized, photo-crosslinkable RLP/ELP constructs: the anticancer ligands were genetically encoded to be presented on the C-terminal, hydrophilic end of the construct with a hydrophilic K_8D_4 linker between the ligand and the ELP block.

overexpressed in growing tumors during angiogenesis 47 and a linear GRGDSPAS octapeptide taken from the recognition site in the FG loop of the Fn3 scaffold that also binds the $\alpha_v \beta_3$ integrin, though with decreased efficacy and specificity. The former has an equilibrium dissociation constant $(K_{\rm d})$ for the $\alpha_v \beta_3$ integrin in the high nanomolar range 59,61 whereas the $K_{\rm d}$ for the $\alpha_v \beta_3$ integrin for the latter is expected in the midmicromolar range based on reports using similar peptide ligands. In a previous work, we showed that the multivalent display of the Fn3 domain on a spherical RLP₄₀–ELP₈₀ micelle can improve its binding avidity for the $\alpha_v \beta_3$ integrin by more than 10-fold compared to the soluble unimer. On the specific can be sufficiently approximately sufficiently sufficien

All constructs also contained a K_8D_4 linker between the ELP block and the ligand that consisted of eight lysine and four aspartic acid residues (Figure 2). This hydrophilic spacer has been shown to greatly improve ligand accessibility on ELP micelles, particularly for short hydrophobic peptide ligands. In addition, introducing a net 4+ charge at the particle—solution interface may also improve the nanoparticles' ability to target the negatively charged cell surface. 65

After successful expression and purification of the fusion constructs (Figure S5), characterization of the corresponding crosslinked nanoparticles by DLS and cryo-TEM showed that the C-terminal presentation of the ligands on the corona of the $RLP_{40,5pAzF}$ – ELP_{80} micelles did not influence their spherical morphology or their stability (Figure S6).

To analyze the in vitro bioactivity of the Tn3-functionalized nanoparticles, we performed cell viability experiments using the colorectal cancer cell line Colo205 that is known to have a high DR5 density.⁶⁶ Cell viability analysis after 24 h of treatment with nanoparticle solutions showed that the uncrosslinked constructs had an EC $_{50}$ of 1.16 μM , whereas the crosslinked analogues were ~5000-fold more potent, with an EC₅₀ of 246 pM (Figure 3). In conjunction with the measured CMC of $\sim 1~\mu M$ (Figure S4), the data strongly suggests that the observed increase in potency for the crosslinked formulation is a direct consequence of preserving multivalent interactions below the CMC. Below $\sim 1 \mu M$, the uncrosslinked micelles disassemble into unimers and lose their activity, whereas the core-crosslinked micelles remain intact and continue to bind their cognate receptors on the cell surface with high avidity, ultimately leading to far greater bioactivity than their uncrosslinked analogues.

These results also suggest that the architecture—format of presentation, ligand spacing, and flexibility—of multivalent ligand presentation has an important role in modulating the avidity as the potency of our crosslinked spherical nanoparticles is decreased compared to that of linear Tn3 oligomers. The estimated ligand density on these nanoparticles is less than 10% compared to the linear oligomers, which might help explain the observed effects. Nevertheless,

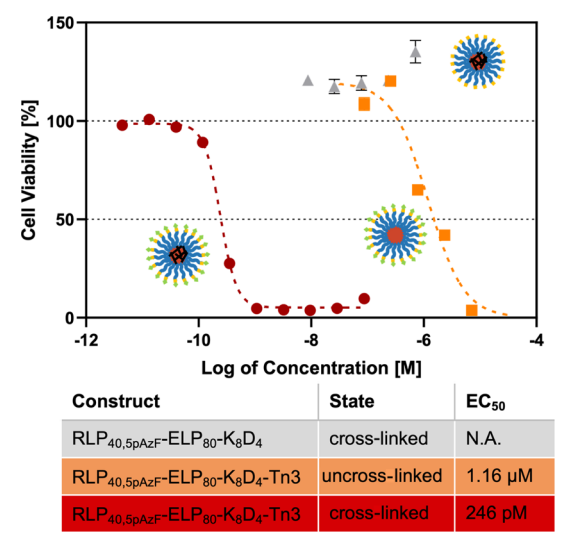


Figure 3. Cell viability experiments for DR5-targeting constructs: cell survival curves for Colo205 cells after coincubation with DR5-targeting constructs over 24 h in complete media showed that the EC_{50} value for the uncrosslinked sample closely matched the CMC of the unfunctionalized RLP/ELP diblock micelles. Photo-crosslinking significantly increased the potency of Tn3-functionalized nanoparticles to concentrations well below the CMC.

our nanoparticles reached a sub-nanomolar EC_{50} value, which is sufficient for most applications. Moreover, experiments with mixed micelles containing both unfunctionalized and Tn3-bearing constructs revealed that the ligand density can be reduced by another 50% without significantly compromising the potency (Figure S7). One could thus envision mixed micelles that present two different moieties that target separate receptors to enhance the targeting specificity and efficacy.

We next investigated the cell internalization of the crosslinked and uncrosslinked nanoparticles that present the integrin-targeting Fn3 and GRGDSPAS ligands. To do so, we conjugated the fluorescent dye Alexa Fluor 488 to the Nterminus of the diblock constructs, and incubated the labeled nanoparticles with an engineered K562 leukemia cell line that had been transfected to express the $\alpha_y \beta_3$ integrin.³⁰ After 2 h of incubation at two different concentrations—3.5 µM and 70 nM, chosen because they bracket the CMC of the uncrosslinked micelles—cellular uptake was visualized by confocal fluorescence microscopy and quantified by flow cytometry. Both methods revealed that nanoparticle crosslinking greatly increases cellular internalization at low concentrations below the CMC (Figure 4): whereas treatment with the uncrosslinked micelles resulted in comparable uptake levels (vs crosslinked samples) at 3.5 μ M, there was almost no detectable uptake of the uncrosslinked micelles at 70 nM, presumably because the monovalent affinity upon nanoparticle

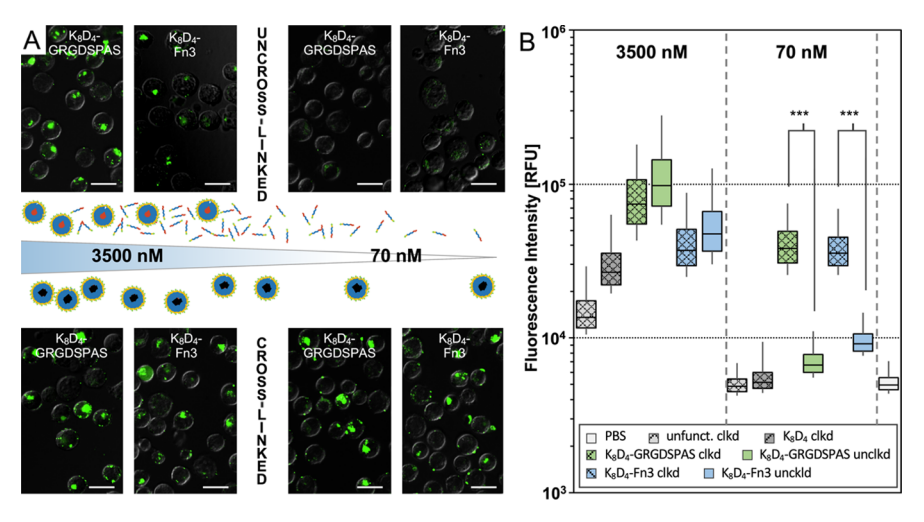


Figure 4. Quantification of cellular uptake for integrin-targeting constructs: (A) representative images of K562 cells after coincubation with AF488-labeled (green), functionalized nanoparticles over 1.5 h in PBS. Scale bars represent 20 μ m. (B) Quantification of cell uptake levels using flow cytometry. Boxes indicate 3rd and 7th percentiles, bars represent 1st and 9th percentiles over >30,000 events. Note that all constructs have a RLP_{40,5pAzF}-ELP₈₀ base and carry the C-terminal functionalization denoted on the respective images or figure legend. See Figures S8–S10 for additional microscopy images and flow cytometry histograms ***p < 0.001 (unpaired Student's t-test).

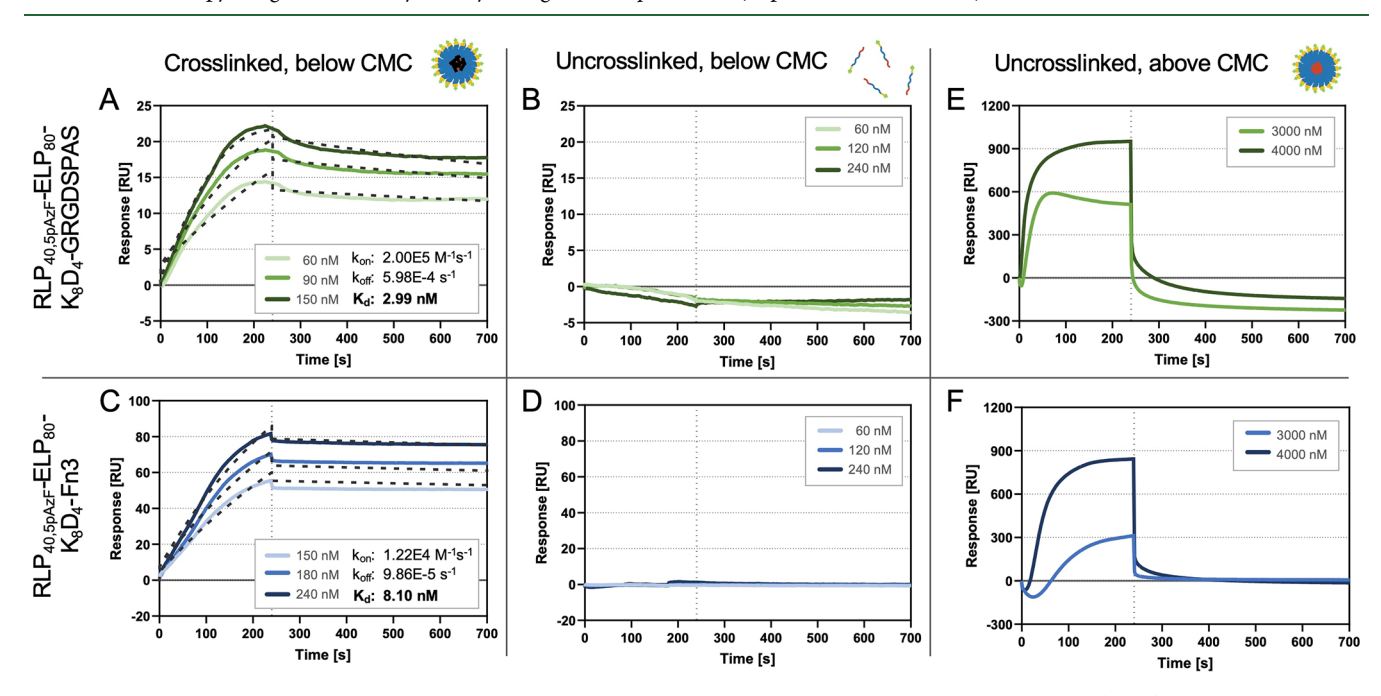


Figure 5. SPR data for the integrin-targeting RLP/ELP diblock polypeptides both above and below their CMC: (A–D) SPR sensorgrams for ligand-functionalized RLP/ELP constructs at concentrations below the CMC, showing that for both ligands integrin-binding is only retained for photo-crosslinked nanoparticles but not for their uncrosslinked analogues. (E,F) SPR sensorgrams at concentrations above the CMC show moderate binding avidities for uncrosslinked, functionalized nanoparticles. Note that the dotted vertical line represents the point at which the buffer was exchanged during the SPR measurement. See Figure S12 for SPR sensorgrams for the untargeted control constructs.

disassembly below the CMC is far too low to lead to efficient receptor-mediated internalization. The crosslinked micelles, on the other hand, showed the same level of uptake at 70 nM as at 3.5 μ M, indicating that even at a 500-fold lower concentration, the avidity of the crosslinked nanoparticles remains intact, thus enabling efficient cell uptake.

Interestingly, the data also strongly indicates that switching from the Fn3 protein ligand to the GRGDSPAS peptide ligand—thereby decreasing the monovalent binding affinity by 2 orders of magnitude—does not significantly compromise the cellular uptake of the crosslinked nanoparticles. Comparison of the uptake by $\alpha_{\nu}\beta_{3}$ integrin-positive and -negative K562 cell

lines showed that high levels of nanoparticle internalization can be predominantly attributed to specific ligand—receptor interactions (Figure S11). Thus, we conclude that in multivalent systems, the monovalent binding affinities of the ligands only have a minor influence on the overall targeting efficacy, which appears to be dominated by ligand valency. These observations are consistent with previous studies showing that the ligand density as well as the ligand-to-receptor ratio are the main drivers of nanoparticle activity. ^{30,67–69} In fact, Maguire *et al.* reported that multivalent, integrin-targeted, recombinant adenoviruses with two different RGD peptides showed no difference in transfection efficiency,

even though the monovalent binding affinities of the ligands differed by more than 100-fold. 70

The findings of the cell uptake experiments were supported by SPR measurements. In general, the experimental layout for these measurements was identical to the uptake experiments: binding kinetics were determined for uncrosslinked and crosslinked nanoparticles at concentrations both above and below the CMC. In agreement with the cell uptake experiments, the uncrosslinked constructs showed moderate binding in the concentrated regime but no detectable binding below the CMC (Figure 5). The crosslinked nanoparticles, on the other hand, showed exceptional binding kinetics in the dilute regime, with the $K_{\rm d}$ values for both ligands in the low nanomolar range, consistent with preservation of their spherical nanoparticle morphology.

As opposed to the uptake experiments, the SPR sensorgrams also indicated some differences between the Fn3- and GRGDSPAS-functionalized nanoparticles: though the overall $K_{\rm d}$ values were quite similar, the $k_{\rm on}$ and $k_{\rm off}$ differed significantly. The lower $k_{\rm off}$ for the Fn3-functionalized particles suggests that they hold onto the integrins more strongly than the GRGDSPAS-carrying micelles, which is expected based on the differences in monovalent binding affinity. Regarding the differences in $k_{\rm on}$, we hypothesize that this is caused by conformational restrictions due to the more complex three-dimensional architecture of the Fn3 protein ligand compared to that of the small GRGDSPAS peptide. The sum of the small GRGDSPAS peptide.

Finally, SPR data was also acquired for the Tn3-functionalized constructs in an analogous manner (Figure S13). As opposed to the integrin-targeting nanoparticles, the SPR measurements revealed that for the DR5-targeted micelles, the uncrosslinked constructs also showed a strong binding at concentrations below the CMC. As the dependency on multivalent display for the Tn3 ligand stems from the downstream trimerization of ligand-bound DR5 receptors rather than the binding process itself, these results are not surprising. With an exceptionally low K_d of 21 pM, the crosslinked nanoparticles showed improved binding by around 3 orders of magnitude compared to the monovalent construct reported by Swers et al. 18 These affinities compare to the ones found for many engineered antibodies and antibody fragments—the current gold standard for high affinity protein ligands. 25,72,73

CONCLUSIONS AND OUTLOOK

In summary, this study demonstrates the great potential of core-crosslinked RLP/ELP nanoparticles in the context of multivalent ligand display. Whereas the self-assembled nanoparticles held together solely by thermodynamic forces immediately became inactive upon dilution below their CMC, their photo-crosslinked analogues retained their activity even after a further 1000-fold dilution.

Our data reinforces the importance of valency on molecular interactions. Though the two $\alpha_v \beta_3$ integrin-targeting ligands we investigated were very different in size, complexity, and monovalent binding affinity, the corresponding nanoparticle formulations demonstrated almost identical cellular internalization rates. Remarkably, with a measured $K_{\rm d}$ of 3 nM, the GRGDSPAS-functionalized, crosslinked nanoparticles exhibited a binding avidity that is more than 1000-fold greater than the monomeric sequence. 62,63 Since our nanoparticles are furthermore expected to have a greatly improved serum half-

life *in vivo*, ⁴¹ they represent a real alternative to antibodies for high-affinity tumor targeting.

In summary, our method enables the creation of monodisperse, highly potent nanoparticles with remarkable stability by recombinant protein expression methods. As the amphiphilic RLP/ELP building block is genetically encoded, peptide and protein ligands can be fused—at the gene level without requiring a separate conjugation step. Furthermore, these diblock polypeptides spontaneously and reliably selfassemble into spherical nanoparticles regardless of their corona modification and without the need for any additional processing. Also, the cores of these nanoparticles can be easily covalently crosslinked by brief UV exposure without the necessary addition of a chemical crosslinker or the removal of any by-products after crosslinking. Finally, by introducing drug conjugation sites into the RLP block that are spatially separated from the pAzF residues to prevent cross-reactivity, the presented platform can easily be expanded to create drugloaded core-crosslinked micelles. This nanoparticle system now sets the stage for future studies that will focus on understanding the impact of ligand presentation and nanoparticle stability on their in vivo pharmacokinetics, tumor accumulation, and ultimately tumor regression.

ASSOCIATED CONTENT

Supporting Information

The Supporting Information is available free of charge at https://pubs.acs.org/doi/10.1021/acs.biomac.1c00897.

Amino acid/genetic sequences, SDS-PAGE gels, flow cytometry histograms as well as additional cryo-TEM images, DLS curves, and SPR sensorgrams (PDF)

AUTHOR INFORMATION

Corresponding Author

Ashutosh Chilkoti — Department of Biomedical Engineering, Duke University, Durham, North Carolina 27708, United States; orcid.org/0000-0002-1569-2228; Email: chilkoti@duke.edu

Authors

Patrick Weber — Tissue Engineering & Biofabrication Laboratory, Department of Health Sciences and Technology, ETH Zurich, 8093 Zurich, Switzerland; Department of Biomedical Engineering, Duke University, Durham, North Carolina 27708, United States; Swiss Nanoscience Institute, University of Basel, 4056 Basel, Switzerland

Michael Dzuricky – Department of Biomedical Engineering, Duke University, Durham, North Carolina 27708, United States; ocid.org/0000-0002-1775-2132

Junseon Min — Department of Biomedical Engineering, Duke University, Durham, North Carolina 27708, United States Irene Jenkins — Department of Biomedical Engineering, Duke University, Durham, North Carolina 27708, United States

Complete contact information is available at: https://pubs.acs.org/10.1021/acs.biomac.1c00897

Author Contributions

The experiments of this study were designed by P.W., M.D., J.M., I.J., and A.C. and performed and analyzed by P.W., M.D., I.J., and J.M. The manuscript was written by P.W., M.D., and A.C. All authors have given approval to the final version of the manuscript.

Funding

This work was supported by the NSF through a DMREF grant (DMR-1729671) to A.C., and the NIH through grant NIH MIRA R35GM127042 to A.C. This work utilized facilities supported in part by the National Science Foundation under Agreement no. DMR-0944772.

Notes

The authors declare no competing financial interest.

ACKNOWLEDGMENTS

We acknowledge the Duke University Shared Materials and Instrumentation Facility for maintaining the cryo-TEM instrument used in this work. Moreover, we would like to thank Prof. Farren J. Isaacs (Yale University, USA) for generously providing both the amber-suppressor C321. Δ A *E. coli* as well as the orthogonal pEVOL vector that were used in this study.

REFERENCES

- (1) Bobo, D.; Robinson, K. J.; Islam, J.; Thurecht, K. J.; Corrie, S. R. Nanoparticle-Based Medicines: A Review of FDA-Approved Materials and Clinical Trials to Date. *Pharm. Res.* **2016**, *33*, 2373–2387.
- (2) Janib, S. M.; Moses, A. S.; MacKay, J. A. Imaging and Drug Delivery Using Theranostic Nanoparticles. *Adv. Drug Delivery Rev.* **2010**, *62*, 1052–1063.
- (3) Davis, S. S.; Washington, C.; West, P.; Illum, L.; Liversidge, G.; Sternson, L.; Kirsh, R. Lipid Emulsions as Drug Delivery Systems. *Ann. N.Y. Acad. Sci.* **1987**, *507*, 75–88.
- (4) Sharma, A.; Sharma, U. S. Liposomes in Drug Delivery: Progress and Limitations. *Int. J. Pharm.* **1997**, *154*, 123–140.
- (5) Allen, T. M.; Cullis, P. R. Liposomal Drug Delivery Systems: From Concept to Clinical Applications. *Adv. Drug Delivery Rev.* **2013**, 65, 36–48
- (6) Mehnert, W.; Mäder, K. Solid Lipid Nanoparticles: Production, Characterization and Applications. *Adv. Drug Delivery Rev.* **2012**, *64*, 83–101.
- (7) Lee, J. S.; Feijen, J. Polymersomes for Drug Delivery: Design, Formation and Characterization. *J. Controlled Release* **2012**, *161*, 473–483
- (8) Liong, M.; Lu, J.; Kovochich, M.; Xia, T.; Ruehm, S. G.; Nel, A. E.; Tamanoi, F.; Zink, J. I. Multifunctional Inorganic Nanoparticles for Imaging, Targeting, and Drug Delivery. *ACS Nano* **2008**, 2, 889–896
- (9) Gillies, E. R.; Fréchet, J. M. J. Dendrimers and Dendritic Polymers in Drug Delivery. *Drug Discovery Today* **2005**, *10*, 35–43.
- (10) Li, S.-D.; Huang, L. Pharmacokinetics and Biodistribution of Nanoparticles. *Mol. Pharm.* **2008**, *5*, 496–504.
- (11) Torchilin, V. Tumor Delivery of Macromolecular Drugs Based on the EPR Effect. *Adv. Drug Delivery Rev.* **2011**, *63*, 131–135.
- (12) Matsumura, Y.; Maeda, H. A New Concept for Macromolecular Therapeutics in Cancer Chemotherapy: Mechanism of Tumoritropic Accumulation of Proteins and the Antitumor Agent Smancs. *Cancer Res.* **1986**, *46*, 6387–6392.
- (13) Ruoslahti, E. Targeting Tumor Vasculature with Homing Peptides from Phage Display. Semin. Cancer Biol. 2000, 10, 435–442.
- (14) Truffi, M.; Colombo, M.; Sorrentino, L.; Pandolfi, L.; Mazzucchelli, S.; Pappalardo, F.; Pacini, C.; Allevi, R.; Bonizzi, A.; Corsi, F.; Prosperi, D. Multivalent Exposure of Trastuzumab on Iron Oxide Nanoparticles Improves Antitumor Potential and Reduces Resistance in HER2-Positive Breast Cancer Cells. *Sci. Rep.* **2018**, *8*, 6563.
- (15) Bae, S.; Ma, K.; Kim, T. H.; Lee, E. S.; Oh, K. T.; Park, E.-S.; Lee, K. C.; Youn, Y. S. Doxorubicin-Loaded Human Serum Albumin Nanoparticles Surface-Modified with TNF-Related Apoptosis-Inducing Ligand and Transferrin for Targeting Multiple Tumor Types. *Biomaterials* **2012**, *33*, 1536–1546.

- (16) Montet, X.; Funovics, M.; Montet-Abou, K.; Weissleder, R.; Josephson, L. Multivalent Effects of RGD Peptides Obtained by Nanoparticle Display. *J. Med. Chem.* **2006**, 49, 6087–6093.
- (17) Han, J. H.; Moon, A. R.; Chang, J. H.; Bae, J.; Choi, J. M.; Lee, S. H.; Kim, T.-H. Potentiation of TRAIL Killing Activity by Multimerization through Isoleucine Zipper Hexamerization Motif. *BMB Rep.* **2016**, *49*, 282–287.
- (18) Swers, J. S.; Grinberg, L.; Wang, L.; Feng, H.; Lekstrom, K.; Carrasco, R.; Xiao, Z.; Inigo, I.; Leow, C. C.; Wu, H.; Tice, D. A.; Baca, M. Multivalent Scaffold Proteins as Superagonists of TRAIL Receptor 2—Induced Apoptosis. *Mol. Cancer Ther.* **2013**, *12*, 1235—1244.
- (19) Banerjee, D.; Liu, A. P.; Voss, N. R.; Schmid, S. L.; Finn, M. G. Multivalent Display and Receptor-Mediated Endocytosis of Transferrin on Virus-Like Particles. *ChemBioChem* **2010**, *11*, 1273–1279.
- (20) Kiessling, L. L.; Lamanna, A. C. Multivalency in Biological Systems. In *Chemical Probes in Biology*; Schneider, M. P., Ed.; NATO Science Series; Springer Netherlands: Dordrecht, 2003; pp 345–357.
- (21) Ranger, M.; Jones, M.-C.; Yessine, M.-A.; Leroux, J.-C. From Well-Defined Diblock Copolymers Prepared by a Versatile Atom Transfer Radical Polymerization Method to Supramolecular Assemblies. J. Polym. Sci., Part A: Polym. Chem. 2001, 39, 3861–3874.
- (22) Van Domeselaar, G. H.; Kwon, G. S.; Andrew, L. C.; Wishart, D. S. Application of Solid Phase Peptide Synthesis to Engineering PEO-Peptide Block Copolymers for Drug Delivery. *Colloids Surf., B* **2003**, *30*, 323–334.
- (23) Xu, J.-P.; Ji, J.; Chen, W.-D.; Shen, J.-C. Novel Biomimetic Polymersomes as Polymer Therapeutics for Drug Delivery. *J. Controlled Release* **2005**, 107, 502–512.
- (24) Lu, J.; Owen, S. C.; Shoichet, M. S. Stability of Self-Assembled Polymeric Micelles in Serum. *Macromolecules* **2011**, *44*, 6002–6008.
- (25) Kennedy, P. J.; Oliveira, C.; Granja, P. L.; Sarmento, B. Monoclonal Antibodies: Technologies for Early Discovery and Engineering. *Crit. Rev. Biotechnol.* **2018**, *38*, 394–408.
- (26) Igawa, T.; Tsunoda, H.; Kuramochi, T.; Sampei, Z.; Ishii, S.; Hattori, K. Engineering the Variable Region of Therapeutic IgG Antibodies. *mAbs* **2011**, *3*, 243–252.
- (27) Ambaye, N. D.; Yu, H. E. Novel Anti-Cancer Candidates from a Combinatorial Peptide Library. *Chem. Biol. Drug Des.* **2021**, *97*, 87–96
- (28) Brown, K. C. Peptidic Tumor Targeting Agents: The Road from Phage Display Peptide Selections to Clinical Applications. *Curr. Pharm. Des.* **2010**, *16*, 1040–1054.
- (29) Pavet, V.; Beyrath, J.; Pardin, C.; Morizot, A.; Lechner, M.-C.; Briand, J.-P.; Wendland, M.; Maison, W.; Fournel, S.; Micheau, O.; Guichard, G.; Gronemeyer, H. Multivalent DR5 Peptides Activate the TRAIL Death Pathway and Exert Tumoricidal Activity. *Cancer Res.* **2010**, *70*, 1101–1110.
- (30) Dzuricky, M.; Xiong, S.; Weber, P.; Chilkoti, A. Avidity and Cell Uptake of Integrin-Targeting Polypeptide Micelles Is Strongly Shape-Dependent. *Nano Lett.* **2019**, *19*, 6124–6132.
- (31) Rijcken, C. J.; Snel, C. J.; Schiffelers, R. M.; van Nostrum, C. F.; Hennink, W. E. Hydrolysable Core-Crosslinked Thermosensitive Polymeric Micelles: Synthesis, Characterisation and in Vivo Studies. *Biomaterials* **2007**, *28*, 5581–5593.
- (32) Li, Y.; Xiao, K.; Luo, J.; Xiao, W.; Lee, J. S.; Gonik, A. M.; Kato, J.; Dong, T. A.; Lam, K. S. Well-Defined, Reversible Disulfide Cross-Linked Micelles for on-Demand Paclitaxel Delivery. *Biomaterials* **2011**, *32*, 6633–6645.
- (33) Li, Y.; Xiao, W.; Xiao, K.; Berti, L.; Luo, J.; Tseng, H. P.; Fung, G.; Lam, K. S. Well-Defined, Reversible Boronate Crosslinked Nanocarriers for Targeted Drug Delivery in Response to Acidic PH Values and Cis-Diols. *Angew. Chem., Int. Ed.* **2012**, *51*, 2864–2869.
- (34) Talelli, M.; Barz, M.; Rijcken, C. J. F.; Kiessling, F.; Hennink, W. E.; Lammers, T. Core-Crosslinked Polymeric Micelles: Principles, Preparation, Biomedical Applications and Clinical Translation. *Nano Today* **2015**, *10*, 93–117.
- (35) Huang, J.; Wu, F.; Yu, Y.; Huang, H.; Zhang, S.; You, J. Lipoic Acid Based Core Cross-Linked Micelles for Multivalent Platforms:

- Design, Synthesis and Application in Bio-Imaging and Drug Delivery. Org. Biomol. Chem. 2017, 15, 4798–4802.
- (36) McDaniel, J. R.; Callahan, D. J.; Chilkoti, A. Drug Delivery to Solid Tumors by Elastin-like Polypeptides. *Adv. Drug Delivery Rev.* **2010**, *62*, 1456–1467.
- (37) Li, L.; Tong, Z.; Jia, X.; Kiick, K. L. Resilin-like Polypeptide Hydrogels Engineered for Versatile Biological Function. *Soft Matter* **2013**, *9*, 665–673.
- (38) Li, L.; Kiick, K. L. Resilin-Based Materials for Biomedical Applications. ACS Macro Lett. 2013, 2, 635–640.
- (39) Urry, D. W.; Parker, T. M.; Reid, M. C.; Gowda, D. C. Biocompatibility of the Bioelastic Materials, Poly(GVGVP) and Its γ -Irradiation Cross-Linked Matrix: Summary of Generic Biological Test Results. *J. Bioact. Compat. Polym.* **1991**, *6*, 263–282.
- (40) Weitzhandler, I.; Dzuricky, M.; Hoffmann, I.; Garcia Quiroz, F.; Gradzielski, M.; Chilkoti, A. Micellar Self-Assembly of Recombinant Resilin-/Elastin-Like Block Copolypeptides. *Biomacromolecules* **2017**, *18*, 2419–2426.
- (41) Costa, S. A.; Simon, J. R.; Amiram, M.; Tang, L.; Zauscher, S.; Brustad, E. M.; Isaacs, F. J.; Chilkoti, A. Photo-Crosslinkable Unnatural Amino Acids Enable Facile Synthesis of Thermoresponsive Nano-to Microgels of Intrinsically Disordered Polypeptides. *Adv. Mater.* **2018**, *30*, 1704878.
- (42) Young, T. S.; Ahmad, I.; Yin, J. A.; Schultz, P. G. An Enhanced System for Unnatural Amino Acid Mutagenesis in E. Coli. *J. Mol. Biol.* **2010**, 395, 361–374.
- (43) Isaacs, F. J.; Carr, P. A.; Wang, H. H.; Lajoie, M. J.; Sterling, B.; Kraal, L.; Tolonen, A. C.; Gianoulis, T. A.; Goodman, D. B.; Reppas, N. B.; Emig, C. J.; Bang, D.; Hwang, S. J.; Jewett, M. C.; Jacobson, J. M.; Church, G. M. Precise Manipulation of Chromosomes in Vivo Enables Genome-Wide Codon Replacement. *Science* **2011**, 333, 348–353
- (44) Lajoie, M. J.; Rovner, A. J.; Goodman, D. B.; Aerni, H.-R.; Haimovich, A. D.; Kuznetsov, G.; Mercer, J. A.; Wang, H. H.; Carr, P. A.; Mosberg, J. A.; Rohland, N.; Schultz, P. G.; Jacobson, J. M.; Rinehart, J.; Church, G. M.; Isaacs, F. J. Genomically Recoded Organisms Expand Biological Functions. *Science* 2013, 342, 357–360.
- (45) Gritsan, N.; Platz, M. Photochemistry of Azides: The Azide/ Nitrene Interface; John Wiley & Sons: Hoboken, NJ, USA, 2010.
- (46) Preston, G. W.; Wilson, A. J. Photo-Induced Covalent Cross-Linking for the Analysis of Biomolecular Interactions. *Chem. Soc. Rev.* **2013**, *42*, 3289–3301.
- (47) Liu, Z.; Wang, F.; Chen, X. Integrin Avβ3-Targeted Cancer Therapy. Drug Dev. Res. 2008, 69, 329–339.
- (48) Gladson, C. L.; Cheresh, D. A. Glioblastoma Expression of Vitronectin and the Alpha v Beta 3 Integrin. Adhesion Mechanism for Transformed Glial Cells. *J. Clin. Invest.* **1991**, *88*, 1924–1932.
- (49) Gasparini, G.; Brooks, P. C.; Biganzoli, E.; Vermeulen, P. B.; Bonoldi, E.; Dirix, L. Y.; Ranieri, G.; Miceli, R.; Cheresh, D. A. Vascular Integrin Alpha(v)Beta3: A New Prognostic Indicator in Breast Cancer. Clin. Cancer Res. 1998, 4, 2625–2634.
- (50) Grzesiak, J. J.; Ho, J. C.; Moossa, A. R.; Bouvet, M. The Integrin-Extracellular Matrix Axis in Pancreatic Cancer. *Pancreas* **2007**, *35*, 293–301.
- (51) Pennarun, B.; Meijer, A.; de Vries, E. G. E.; Kleibeuker, J. H.; Kruyt, F.; de Jong, S. Playing the DISC: Turning on TRAIL Death Receptor-Mediated Apoptosis in Cancer. *Biochim. Biophys. Acta, Rev. Cancer* **2010**, *1805*, 123–140.
- (52) McDaniel, J. R.; MacKay, J. A.; Quiroz, F. G.; Chilkoti, A. Recursive Directional Ligation by Plasmid Reconstruction Allows Rapid and Seamless Cloning of Oligomeric Genes. *Biomacromolecules* **2010**, *11*, 944–952.
- (53) Meyer, D. E.; Chilkoti, A. Purification of Recombinant Proteins by Fusion with Thermally-Responsive Polypeptides. *Nat. Biotechnol.* **1999**, *17*, 1112–1115.
- (54) Pan, L.; Fu, T.-M.; Zhao, W.; Zhao, L.; Chen, W.; Qiu, C.; Liu, W.; Liu, Z.; Piai, A.; Fu, Q.; Chen, S.; Wu, H.; Chou, J. J. Higher-Order Clustering of the Transmembrane Anchor of DR5 Drives Signaling. *Cell* 2019, 176, 1477–1489.e14.

- (55) Manzari, M. T.; Anderson, G. R.; Lin, K. H.; Soderquist, R. S.; Çakir, M.; Zhang, M.; Moore, C. E.; Skelton, R. N.; Fèvre, M.; Li, X.; Bellucci, J. J.; Wardell, S. E.; Costa, S. A.; Wood, K. C.; Chilkoti, A. Genomically Informed Small-Molecule Drugs Overcome Resistance to a Sustained-Release Formulation of an Engineered Death Receptor Agonist in Patient-Derived Tumor Models. *Sci. Adv.* **2019**, *5*, No. eaaw9162.
- (56) Ruoslahti, E. Rgd and Other Recognition Sequences for Integrins. Annu. Rev. Cell Dev. Biol. 1996, 12, 697-715.
- (57) Welsh, D. J.; Smith, D. K. Comparing Dendritic and Self-Assembly Strategies to Multivalency—RGD Peptide —Integrin Interactions. *Org. Biomol. Chem.* **2011**, *9*, 4795–4801.
- (58) Raposo Moreira Dias, A.; Pina, A.; Dal Corso, A.; Arosio, D.; Belvisi, L.; Pignataro, L.; Caruso, M.; Gennari, C. Multivalency Increases the Binding Strength of RGD Peptidomimetic-Paclitaxel Conjugates to Integrin AV β 3. *Chem.—Eur. J.* **2017**, 23, 14410–14415.
- (59) Richards, J.; Miller, M.; Abend, J.; Koide, A.; Koide, S.; Dewhurst, S. Engineered Fibronectin Type III Domain with a RGDWXE Sequence Binds with Enhanced Affinity and Specificity to Human $\text{Av}\beta3$ Integrin. *J. Mol. Biol.* **2003**, 326, 1475–1488.
- (60) Main, A. L.; Harvey, T. S.; Baron, M.; Boyd, J.; Campbell, I. D. The Three-Dimensional Structure of the Tenth Type III Module of Fibronectin: An Insight into RGD-Mediated Interactions. *Cell* **1992**, 71, 671–678.
- (61) Bowditch, R. D.; Hariharan, M.; Tominna, E. F.; Smith, J. W.; Yamada, K. M.; Getzoff, E. D.; Ginsberg, M. H. Identification of a Novel Integrin Binding Site in Fibronectin. Differential Utilization by Beta 3 Integrins. *J. Biol. Chem.* **1994**, 269, 10856–10863.
- (62) Pierschbacher, M. D.; Ruoslahti, E. Cell Attachment Activity of Fibronectin Can Be Duplicated by Small Synthetic Fragments of the Molecule. *Nature* **1984**, *309*, 30–33.
- (63) Mohri, H.; Hashimoto, Y.; Ohba, M.; Kumagai, H.; Ohkubo, T. Novel effect of cyclicization of the Arg-Gly-Asp-containing peptide on vitronectin binding to platelets. *Am. J. Hematol.* **1991**, *37*, 14–19.
- (64) Wang, J.; Dzuricky, M.; Chilkoti, A. The Weak Link: Optimization of the Ligand–Nanoparticle Interface To Enhance Cancer Cell Targeting by Polymer Micelles. *Nano Lett.* **2017**, *17*, 5995–6005
- (65) Harush-Frenkel, O.; Debotton, N.; Benita, S.; Altschuler, Y. Targeting of Nanoparticles to the Clathrin-Mediated Endocytic Pathway. *Biochem. Biophys. Res. Commun.* **2007**, 353, 26–32.
- (66) Szegezdi, E.; O'Reilly, A.; Davy, Y.; Vawda, R.; Taylor, D. L.; Murphy, M.; Samali, A.; Mehmet, H. Stem Cells Are Resistant to TRAIL Receptor-Mediated Apoptosis. *J. Cell. Mol. Med.* **2009**, *13*, 4409–4414.
- (67) Wang, J.; Min, J.; Eghtesadi, S. A.; Kane, R. S.; Chilkoti, A. Quantitative Study of the Interaction of Multivalent Ligand-Modified Nanoparticles with Breast Cancer Cells with Tunable Receptor Density. *ACS Nano* **2020**, *14*, 372–383.
- (68) Gestwicki, J. E.; Cairo, C. W.; Strong, L. E.; Oetjen, K. A.; Kiessling, L. L. Influencing Receptor-Ligand Binding Mechanisms with Multivalent Ligand Architecture. *J. Am. Chem. Soc.* **2002**, *124*, 14922–14933.
- (69) Wang, J.; Tian, S.; Petros, R. A.; Napier, M. E.; DeSimone, J. M. The Complex Role of Multivalency in Nanoparticles Targeting the Transferrin Receptor for Cancer Therapies. *J. Am. Chem. Soc.* **2010**, 132, 11306–11313.
- (70) Maguire, C. A.; Sapinoro, R.; Girgis, N.; Rodriguez-Colon, S. M.; Ramirez, S. H.; Williams, J.; Dewhurst, S. Recombinant Adenovirus Type 5 Vectors That Target DC-SIGN, ChemR23 and Av β 3 Integrin Efficiently Transduce Human Dendritic Cells and Enhance Presentation of Vectored Antigens. *Vaccine* **2006**, *24*, 671–682
- (71) Alsallaq, R.; Zhou, H.-X. Electrostatic rate enhancement and transient complex of protein—protein association. *Proteins: Struct., Funct., Bioinf.* **2008**, 71, 320–335.
- (72) Lu, D.; Shen, J.; Vil, M. D.; Zhang, H.; Jimenez, X.; Bohlen, P.; Witte, L.; Zhu, Z. Tailoring in Vitro Selection for a Picomolar Affinity

Human Antibody Directed against Vascular Endothelial Growth Factor Receptor 2 for Enhanced Neutralizing Activity. *J. Biol. Chem.* **2003**, 278, 43496–43507. (73) Rappazzo, C. G.; Tse, L. V.; Kaku, C. I.; Wrapp, D.; Sakharkar,

(73) Rappazzo, C. G.; Tse, L. V.; Kaku, C. I.; Wrapp, D.; Sakharkar, M.; Huang, D.; Deveau, L. M.; Yockachonis, T. J.; Herbert, A. S.; Battles, M. B.; O'Brien, C. M.; Brown, M. E.; Geoghegan, J. C.; Belk, J.; Peng, L.; Yang, L.; Hou, Y.; Scobey, T. D.; Burton, D. R.; Nemazee, D.; Dye, J. M.; Voss, J. E.; Gunn, B. M.; McLellan, J. S.; Baric, R. S.; Gralinski, L. E.; Walker, L. M. Broad and Potent Activity against SARS-like Viruses by an Engineered Human Monoclonal Antibody. *Science* 2021, 371, 823–829.